High-Speed Target Location Based on Photoelectric Imaging and Laser Ranging with Fast Steering Mirror Deflection

Kui Shi [1,2], Hongtao Yang [2,*], Jianwei Peng [1,2], Yingjun Ma [1,2] and Hongwei Zhang [2]

1   University of Chinese Academy of Sciences, Beijing 100049, China; shikui@opt.ac.cn (K.S.);
    pengjianwei@opt.ac.cn (J.P.); mayingjun@opt.ac.cn (Y.M.)
2   Xi'an Institute of Optics and Precision Mechanics, Chinese Academy of Sciences, Xi'an 710119, China;
    zhanghongwei@opt.ac.cn
*   Correspondence: yanght@opt.ac.cn

Abstract: There is an increasing number of spacecrafts in orbit, and the collision impact of high-speed moving targets, such as space debris, can cause fatal damage to these spacecrafts. It has become increasingly important to rapidly and accurately locate high-speed moving targets in space. In this study, we designed a visible-light telephoto camera for observing high-speed moving targets and a laser rangefinder for measuring the precise distance of these targets, and we proposed a method of using fast steering mirror deflection to quickly direct the emitted laser towards such targets and measure the distance. Based on the principle of photographic imaging and the precise distance of targets, a collinear equation and a spatial target location model based on the internal and external orientation elements of the camera and the target distance were established, and the principle of target location and the method for calculating target point coordinates were determined. We analyzed the composition of target point location error and derived an equation for calculating such errors. Based on the actual values of various error components and the error synthesis theory, the accuracy of target location was calculated to be 26.5 m when the target distance is 30 km (the relative velocity is 8 km/s and the velocity component perpendicular to the camera's optical axis is less than 3.75 km/s). This study provides a theoretical basis and a method for solving the practical needs of quickly locating high-speed moving targets in space and proposes specific measures to improve target location accuracy.

Keywords: high-speed targets; laser ranging; target location; collinear equation; fast steering mirror; long-focus camera; location error

1. Introduction

Currently, there is an increasing amount of space debris and an explosive growth in the number of spacecrafts in orbit. By accurately locating high-speed moving debris targets in space and obtaining their orientation, distance, and other characteristics, it is possible to record and predict the trajectory of debris movement, enabling the spacecraft (satellite, etc.) to make effective maneuvering and avoid collision, thus providing a strong basis for ensuring the safety of spacecraft. Space debris targets are generally small in size and have fast relative motion speeds. How to detect them at a distance (20~40 km) and effectively identify, quickly locate, and track them is a technical challenge worthy of further research [1].

Xueying Wang and other researchers at the University of National Defense Technology in China aimed to address the short observable time of moving targets in Geostationary Earth Orbit (GEO) using space-based optical monitoring systems [2]. They used standard

GEO altitude as a constraint condition and assumed that targets in GEO would move at a constant speed in short-arc observations. They solved the equation formulated based on the position and angle of the observation platform and the space sphere with a height of 35,786 km from the ground and took the reasonable solution as the initial value of the position of the space-moving target. Then, they used the least squares method to fit the precise position of the moving target.

Yinghao Wu from Nanjing University of Aeronautics and Astronautics in China proposed a target location algorithm based on dual line-of-sight cooperative angle measurement to solve the problem of target location in the process of approaching non-cooperative irregular targets in space and improved the accuracy of target location by optimizing the approaching form of binary stars. A dual-star cooperative location scheme using only line-of-sight measurement was proposed, and a target location algorithm based on an extended Kalman filter was designed [3].

Wu et al. proposed a monostation passive target location method based on infrared quantitative detection, based on high-resolution infrared tracking systems, which measure the target temperature and angle, and the law that target temperature changes with height. They established the theoretical model of target location, which comprehensively considers the factors of temperature retrieval, aerodynamic heating, and atmosphere. They conducted the location experiment with the developed high-resolution infrared tracking system [4].

For aviation electro-optical equipment that integrates cameras and laser rangefinders, accurate position information of ground targets can be calculated using camera images, camera internal and external orientation elements, and target distance [5]. This method has been applied in many aviation optoelectronic devices for ground target location, but it has not yet been applied in spacecraft for space target location [6].

Based on the application demand of preventing space debris from colliding with and causing serious damage to its own spacecraft, this paper studies a fast location technology for space targets. When space debris is found approaching its own spacecraft through a camera with a large field of view or radar, it can achieve observation and precise location of unknown space debris targets. This study designed a visible-light telephoto high-resolution camera to observe high-speed moving targets in space, designed a laser rangefinder to accurately measure the distance of such targets, and proposed using the deflection of a fast steering mirror (FSM) to enable the emitted laser to quickly point at the high-speed targets and complete the distance measurement. Based on the principle of photographic imaging for target image acquisition and the precise distance of the targets, a collinear equation and a spatial target location model based on the internal and external orientation elements of the camera and the target distance were established. A method for calculating the geographic coordinates of the target point was derived, and the error of the target location method was analyzed and calculated [7].

2. Establishment of High-Speed Target Location Model

2.1. Establishment of Coordinate System and Definition of Internal and External Orientation Elements

A spacecraft rotates around Earth at a certain height above the ground, with the reference center W of the spacecraft as the origin and the east, north, and sky above the spacecraft's position as the *X*-, *Y*-, and *Z*-axes, respectively, which are used to establish a spacecraft coordinate system W-xyz. The coordinates of target point *A* in the spacecraft coordinate system W-xyz are (X_A, Y_A, and Z_A).

In the target location model established in this study, the coordinate systems include the spacecraft coordinate system W-xyz, the image spatial auxiliary coordinate system F-xyz, the image coordinate system (*x*, *y*), and the photography coordinate system C-xyz.

The origin of the image spatial auxiliary coordinate system F-xyz is the camera photography center C, and the coordinate axis direction is the same as the corresponding axis direction of the spacecraft coordinate system. In a camera image, an image coordinate system is established with the image center O as the origin and the x- and y-axes aligned with the rows and columns of the image, respectively. The origin of the photography coordinate system C-xyz is the camera photography center C; the z-axis is the main optical axis of the camera and points towards the observed target; and the x- and y-axes are parallel and in the same directions as the x- and y-axes of the image coordinate system, respectively. The x-, y-, and z-axes follow the right-hand rule. The intersection point O' between the z-axis (the main optical axis) of the photography coordinate system C-xyz and the camera image is the principal point of the camera. The coordinates of O' in the image coordinate system are (x_0, y_0) [8].

The internal orientation elements of the camera are represented by $(x_0, y_0, \text{and } f)$, with f representing the focal length of the camera. The position of the photography center point C of the camera in the spacecraft coordinate system W-xyz is $(X_C, Y_C, \text{and } Z_C)$; the camera pose angle elements are $(\varphi, \omega, \text{and } k)$, and the pitch angle φ, roll angle ω, and yaw angle k are measured by the spacecraft pose measurement system based on star sensors. Therefore, $(X_C, Y_C, Z_C, \varphi, \omega, \text{and } k)$ are the external orientation elements of the image [9].

2.2. Coordinate System Establishment and Transformation

As shown in Figure 1, a represents the pixel location of target A in the image. Point a has a coordinate position of $(x \text{ and } y)$ in the image coordinate system and a coordinate position of $(x, y, \text{and } -f)$ in the photography coordinate system. The photography center point C of the camera has coordinates of $(X_C, Y_C, \text{and } Z_C)$ in the spacecraft coordinate system [10].
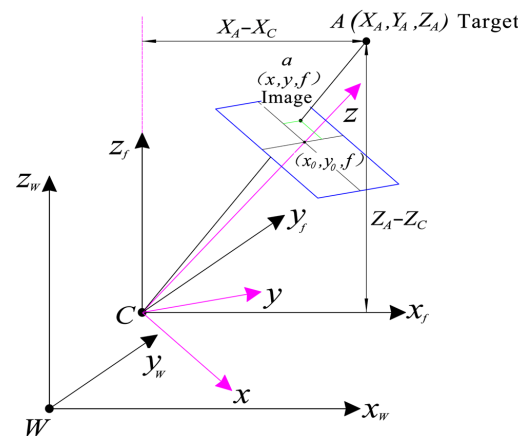

Figure 1. Principle of photographic imaging of targets.

The coordinates of point a in the image spatial auxiliary coordinate system F-xyz are $(X_{af}, Y_{af} \text{ and } Z_{af})$. As shown in Figure 1, rotating the image spatial auxiliary coordinate system F-xyz by the angles of φ, ω, and k on the y-axis, x-axis, and z-axis, respectively, yields the photographic coordinate system C-xyz [11].

Thus,

$$\begin{pmatrix} X_{af} \\ Y_{af} \\ Z_{af} \end{pmatrix} = \begin{bmatrix} \cos\phi & 0 & -\sin\phi \\ 0 & 1 & 0 \\ \sin\phi & 0 & \cos\phi \end{bmatrix} \cdot \begin{bmatrix} 1 & 0 & 0 \\ 0 & \cos\omega & -\sin\omega \\ 0 & \sin\omega & \cos\omega \end{bmatrix} \cdot \begin{bmatrix} \cos k & -\sin k & 0 \\ \sin k & \cos k & 0 \\ 0 & 0 & 1 \end{bmatrix} \cdot \begin{pmatrix} x - x_0 \\ y - y_0 \\ -f \end{pmatrix} \quad (1)$$

Then, according to [12],

$$\begin{pmatrix} X_{af} \\ Y_{af} \\ Z_{af} \end{pmatrix} = \begin{bmatrix} a_{11} & a_{12} & a_{13} \\ a_{21} & a_{22} & a_{23} \\ a_{31} & a_{32} & a_{33} \end{bmatrix} \cdot \begin{pmatrix} x - x_0 \\ y - y_0 \\ -f \end{pmatrix} \tag{2}$$

where

$$\begin{cases} a_{11} = \cos\phi\cos k - \sin\phi\sin\omega\sin k \\ a_{21} = \cos\omega\sin k \\ a_{31} = \sin\phi\cos k + \cos\phi\sin\omega\sin k \\ a_{12} = -\cos\phi\sin k - \sin\phi\sin\omega\cos k \\ a_{22} = \cos\omega\cos k \\ a_{32} = -\sin\phi\sin k + \cos\phi\sin\omega\cos k \\ a_{13} = -\sin\phi\cos\omega \\ a_{23} = -\sin\omega \\ a_{33} = \cos\phi\cos\omega \end{cases} \tag{3}$$

As shown in Figure 1, the direction of each coordinate axis in the image spatial auxiliary coordinate system is the same as that of the corresponding axis in the spacecraft coordinate system, and the origin of the image spatial auxiliary coordinate system is the photography center point C. Therefore, based on the geometric relationship of similar triangles in the spacecraft coordinate system, the following equation can be obtained [13]:

$$\frac{X_A - X_C}{X_{af}} = \frac{Y_A - Y_C}{Y_{af}} = \frac{Z_A - Z_C}{Z_{af}} \tag{4}$$

The collinear equation for photogrammetry obtained by combining Equations (2) and (4) is as follows:

$$\begin{cases} \frac{X_A - X_C}{Z_A - Z_C} = \frac{a_{11}(x-x_0)+a_{12}(y-y_0)-a_{13}f}{a_{31}(x-x_0)+a_{32}(y-y_0)-a_{33}f} \\ \frac{Y_A - Y_C}{Z_A - Z_C} = \frac{a_{21}(x-x_0)+a_{22}(y-y_0)-a_{23}f}{a_{31}(x-x_0)+a_{32}(y-y_0)-a_{33}f} \end{cases} \tag{5}$$

2.3. Laser Ranging Using FSM Deflection

Space targets move at a high speed, with their speed ranging from 6 km/s to 8 km/s. When a target appears within the camera's field of view, it is necessary to quickly complete laser ranging and target location in order to perform effective maneuvering of the spacecraft and avoid collision in a timely manner.

The optical axis of a laser rangefinder is usually parallel to the main optical axis of the camera, and in this case, the laser rangefinder can only measure the distance of the target at the center point of the camera's field of view. The actual target that needs to be measured is usually not at the center of the camera's field of view, making it impossible to measure the target distance. In many similar aviation optoelectronic devices, a two-dimensional turntable is used to rotate the camera and the laser rangefinder as a whole in two dimensions so that the optical axis points towards the target to be measured. After the optical axes of the camera and laser rangefinder are rotated, the target is located at the center point of the camera's field of view, allowing distance measurement and location of the target point to be achieved. For aerospace optoelectronic equipment, the method of using a two-dimensional turntable will significantly increase the volume and weight of the system, and the rotation speed of a two-dimensional turntable is relatively slow, which may not necessarily meet the measurement requirements of high-speed moving targets.

This study innovatively proposes adding an FSM in front of the optical axis of the laser rangefinder to achieve rapid deflection of the laser direction and point it towards a high-speed moving target. Therefore, target ranging in a timely manner is achieved [14].

The sight angle of the target that the FSM needs to deflect is divided into the azimuth angle and elevation angle. The azimuth angle is k_{laser}, and the elevation angle is φ_{laser}. According to the imaging principle, the following can be concluded:

$$
\begin{aligned}
k_{laser} &= \arctan\frac{x-x_0}{f} \\
\phi_{laser} &= \arctan\frac{y-y_0}{f}
\end{aligned}
\tag{6}
$$

If the distance between the target and the observation point measured by the laser rangefinder is L, then the following expression is used:

$$
L = \sqrt{(X_A - X_C)^2 + (Y_A - Y_C)^2 + (Z_A - Z_C)^2}
\tag{7}
$$

2.4. Calculation of Target Point Position

By combining Equations (5) and (7), three equations with three unknowns can be obtained, and the unique solutions of the three unknowns can be derived, which are the position coordinates of the target point (X_A, Y_A, Z_A).

The following is set up:

$$
\begin{cases}
N = a_{11}(x - x_0) + a_{12}(y - y_0) - a_{13}f \\
P = a_{21}(x - x_0) + a_{22}(y - y_0) - a_{23}f \\
Q = a_{31}(x - x_0) + a_{32}(y - y_0) - a_{33}f
\end{cases}
\tag{8}
$$

According to Equation (5), then

$$
\begin{cases}
Y_A - Y_C = \frac{P}{N}(X_A - X_C) \\
Z_A - Z_C = \frac{Q}{N}(X_A - X_C)
\end{cases}
\tag{9}
$$

By combining Equations (7) and (9), it can be concluded that

$$
\begin{cases}
X_A = \frac{N}{\sqrt{N^2+P^2+Q^2}}L + X_C \\
Y_A = \frac{P}{\sqrt{N^2+P^2+Q^2}}L + Y_C \\
Z_A = \frac{Q}{\sqrt{N^2+P^2+Q^2}}L + Z_C
\end{cases}
\tag{10}
$$

where X_A, Y_A, and Z_A are the position coordinates of the target point, which need to be obtained to achieve target location.

3. Design of High-Resolution Long-Focus Camera

The relative motion speed between the satellite itself and the target is about 8 km/s, and the time required for the maneuvering avoidance action is about 3 s. Considering the time required for target recognition and location, the target position must be known at least when the target distance is 30 km.

To clearly observe space debris targets at a distance of 30 km, a high-resolution telephoto camera was designed. To enable such targets to be recognized, the number of pixels occupied by a target with a diameter of 0.1 m in the camera image should not be less than 1 (at a distance of 30 km). A pixel represents 0.12 m after leaving a sufficient design margin, and the resolution of the telephoto camera was set to be 0.12 m@ 30 km.

The imaging resolution mainly depends on the detector pixel size (defined as *s*, unit: μm), the focal length of the optical lens (defined as *f*, unit: mm), and the imaging distance

(defined as *L*, unit: km). *R* represents the imaging resolution (unit: m), so *R*, *s*, *f*, and *L* exhibit the following relationship:

$$\frac{s}{f} = \frac{R}{L} \tag{11}$$

where *R* is 0.12 m, the imaging distance *L* is 30 km, the number of selected detector pixels is 4096 × 3000, and the pixel size *s* is 3.45 μm × 3.45 μm. Therefore, the focal length of the optical system is calculated as follows:

$$f = \frac{s \times L}{R} = 862.5 \text{ mm} \tag{12}$$

3.1. Design of Optical System for High-Resolution Telephoto Camera

According to the requirements of the camera in actual use and technical specifications, the optical system design specifications are as follows:

➢ Spectral range: 450~650 nm
➢ Focal length: ≥862.5 mm

Based on the above optical parameters, the optical system was designed, and the results have been provided in [15]. Figure 2 shows the high-resolution optical system.
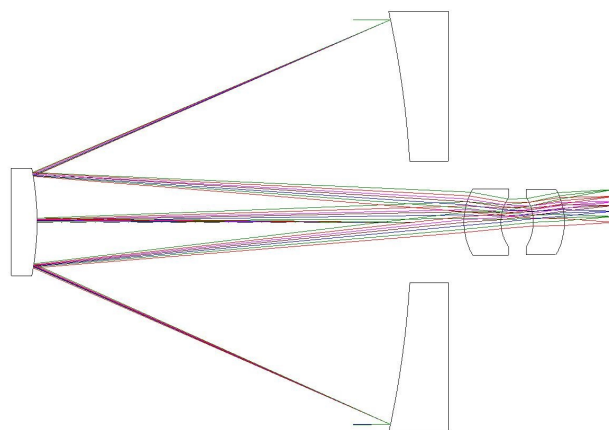
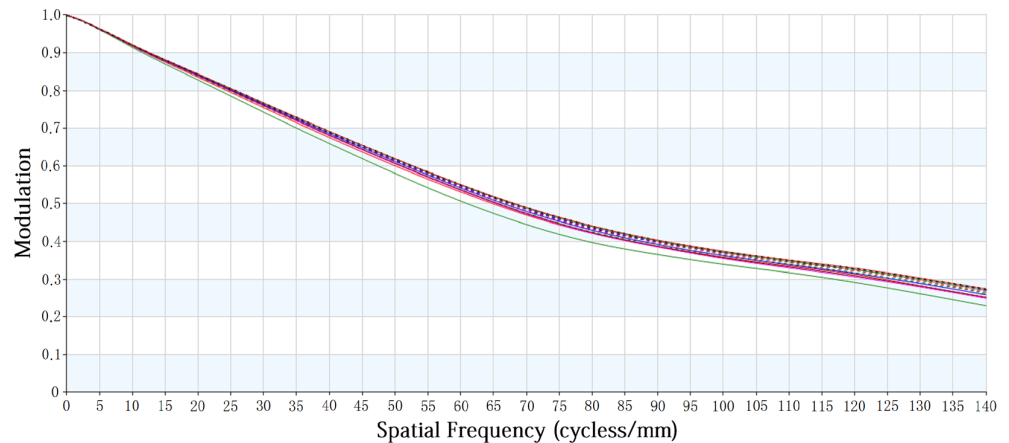**Figure 2.** High-resolution optical system.

The camera optical system adopts the form of a Ritchey–Chrétien (RC) optical system, and the optical material of the primary and secondary mirrors is microcrystalline glass. The reflecting surfaces of the primary and secondary mirrors are both aspherical surfaces, and the distance from the center point of the secondary mirror's reflecting surface to the left surface of the primary mirror's edge is 98.35 mm. Table 1 shows the design results of the optical system.

Table 1. Optical system parameters.

Items	Design Results
Spectral range	450~650 nm
Detector pixel	4096 × 3000, pixel size is 3.45 μm × 3.45 μm
Field of view	0.92° × 0.68°
Focal length	862.5 mm
Relative aperture	F7.85
Distortion	≤2%
Central blocking ratio	0.3
Primary mirror aperture	Φ110 mm
Secondary mirror aperture	Φ27 mm
Total length of optical system	157 mm

The Modulation Transfer Function (MTF) of an optical system can comprehensively reflect its imaging quality and is an important basis for evaluating imaging quality. According to the pixel size (3.45 μm × 3.45 μm) of the Complementary Metal–Oxide–Semiconductor (CMOS) detector, MTF is calculated up to a spatial frequency of 140 lp/mm [16].

Figure 3 shows the MTF curve of the optical system, at the highest spatial frequency of the detector (140 lp/mm), the MTF of the optical system is better than 0.2 (140 lp/mm in the whole field of view (FOV)), and the imaging quality of the optical system is excellent.

Figure 3. MTF curve of the optical system.

### 3.2. Structural Design of High-Resolution Telephoto Camera

The setting of an external light shield is one of the main measures to suppress stray light in optical systems, allowing only a certain level of limited stray light to enter the optical system. As shown in Figure 4, the light shading angle determines the length of the camera's external light shield. The design value for a strong light shading angle of the telephoto camera's optical system is 30°, and the external light shield length reaches 50 mm.
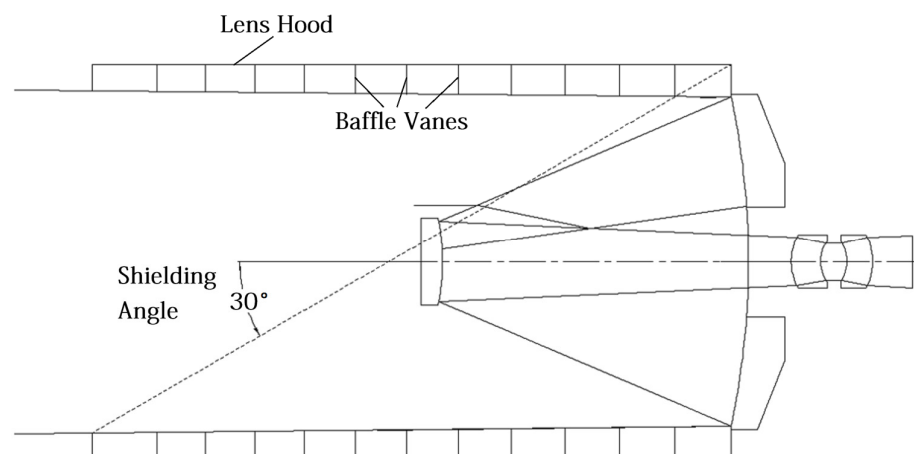
Figure 4. Schematic diagram of the light shading angle in the optical system.

A low level of stray light and the use of high-reliability optical objective lenses are the core components that ensure the imaging quality and effect of the camera. The lens component adopts a Cassegrain structure, which is mainly composed of a primary mirror component, a secondary mirror component, a group of correction mirrors, and an external light shield. The mechanical structure design result of the high-resolution optical objective lens with a long focal length is shown in Figure 5.
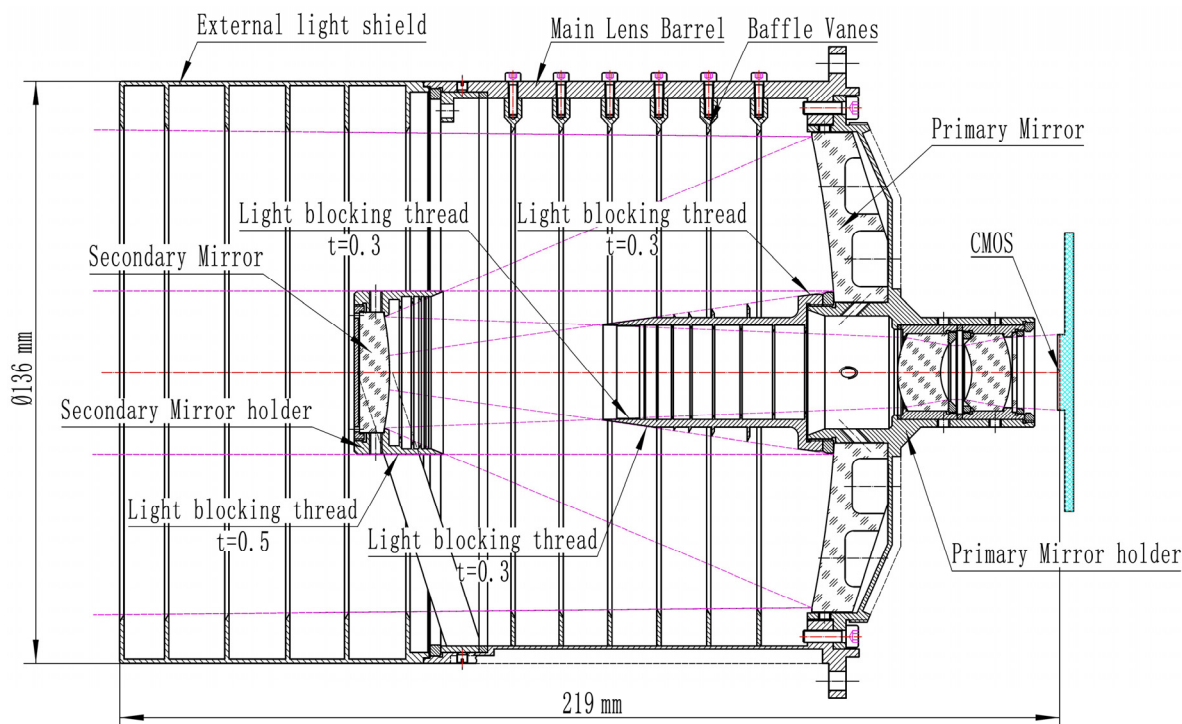
Figure 5. Structural composition of the optical objective lens.

Within the temperature range of the system specifications, in order to ensure that the structural stress and deformation caused by temperature changes will not have a serious impact on imaging quality, it is necessary to use suitable structural materials to reliably obtain excellent images. In this design, the main lens barrel is made of non-expanding steel material Invar 4J32, the primary mirror holder and primary mirror fixing ring are made of titanium alloy TC4, the secondary mirror holder and secondary mirror fixing ring are made of titanium alloy TC4, and all the frames and fixing rings of the correction mirrors are made of titanium alloy TC4, too. To minimize the weight of the system, the external light shield is made of low-density, high-strength magnesium alloy MB15.

Figure 6 shows the image of the camera's optical objective lens.

Figure 6. Image of the camera's optical objective lens.

4. Design of Laser Rangefinder

The main components of a laser rangefinder include a laser-receiving unit, a laser emitting unit, a high-speed deflection mirror system, and a high-repetition-rate fiber laser.

Figure 7 shows a schematic diagram of the composition of the target location system. The high-resolution long-focus camera and the laser-receiving unit are installed on the upper side of the load plate; the optical lens for laser collimation and the fiber laser are installed on the lower side of the load plate; and the high-speed deflection mirror is fixed in the outgoing light path of the optical lens for laser collimation. The detector for completing laser reception is an Avalanche Photodiode (APD) device.
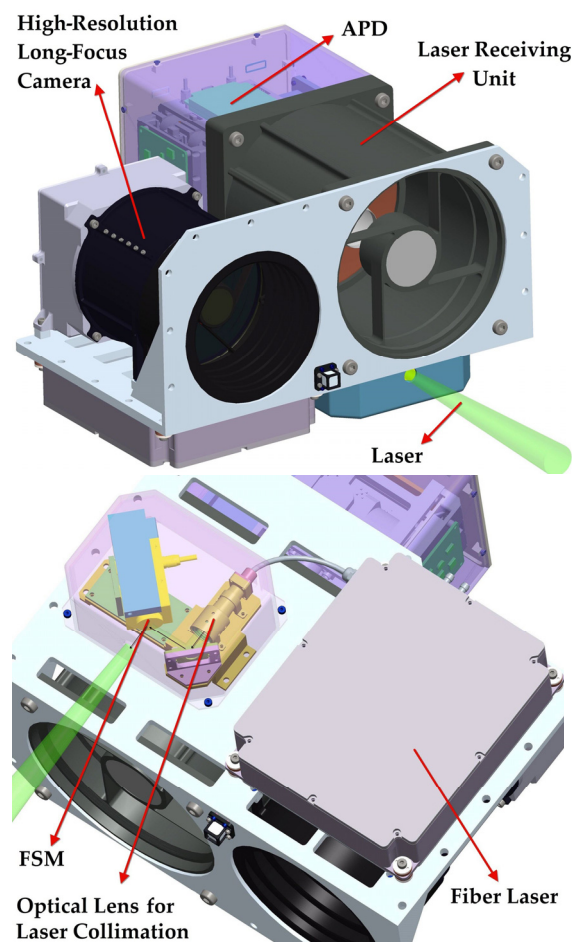
Figure 7. Structural composition diagram of the target location system.

The specifications for the laser rangefinder are as follows [17]:

(1) Laser ranging distance: ≥30 km @ Laser Radar Cross Section (LRCS) = 0.05 m^2.
(2) Laser ranging accuracy (1σ): ≤14 m@ 30 km.
(3) Laser technical specifications:

    (a) Working form: all fiber laser;
    (b) Center wavelength: 1064 nm ± 0.3 nm, with line width of ±3 nm;
    (c) Working mode: pulse;
    (d) Pulse energy: ≥0.5 mJ;
    (e) Pulse repetition frequency: 4000 Hz.

The waist diameter of the laser pulse output from the fiber laser is 31 μm (ω_0 represents the waist radius of the laser pulse output from the fiber laser, so ω_0 is 15.5 μm), with a

divergence angle of 3.5° and λ = 1064 nm. The required divergence angle after collimation is θ_t = 0.2 mrad. The optical lens parameters are calculated as follows [18]:

The waist radius ω_1 of the laser pulse after passing through the optical lens is expressed as follows:

$$\omega_1 = \frac{2\lambda}{\pi\theta_t} = \frac{2 \times 1064 \text{ nm}}{\pi \times 0.2 \text{ mrad}} = 3.387 \text{ mm} \tag{13}$$

The focal length of the optical lens for laser collimation is expressed as follows:

$$f' = \frac{\pi\omega_0\omega_1}{\lambda} = \frac{\pi \times 15.5 \times 10^{-3} \text{ mm} \times 3.387 \text{ mm}}{1.064 \times 10^{-3} \text{ mm}} = 155 \text{ mm} \tag{14}$$

It is necessary to leave a certain design margin with a focal length design value of 160 mm. If the divergence angle of the laser pulse is 3.5°, the image square aperture angle of the beam expansion system needs to be $\geq 3.5°$, and the image square aperture angle of the beam expansion system is set to be $2u$ = 3.7°. Therefore, the entrance pupil diameter of the optical lens is calculated as follows:

$$D = 2f' \tan u \approx 10.3 \text{ mm} \tag{15}$$

The entrance pupil diameter of the optical lens should be $\geq 2\omega_1$; therefore, the entrance pupil diameter of the optical lens is set as D = 10.3 mm.

To ensure that the laser beam accurately illuminates the target, the laser beam divergence angle must cover the target indication accuracy of the high-resolution observation camera, the pointing accuracy of the high-speed deflection mirror, and the flare angle of the target. Therefore, the relationship between the laser beam divergence angle and the overall pointing error, the flare angle of the target, is as follows:

$$\theta_t \geq 2(\sigma + \theta) = 2\sigma + 2\theta \tag{16}$$

where θ_t is the laser beam divergence angle, θ is the flare angle of the target, and σ is the overall pointing error (the root mean square error, which is equal to the root mean square of the target indication accuracy of the high-resolution observation camera, which is 0.017 mrad (0.001 degree), and the FSM pointing accuracy, which is 0.02 mrad). The flare angle θ of a target whose size is 1 m at a distance of 30 km relative to the detector is about 0.033 mrad. Then, the laser beam divergence angle θ_t is calculated as follows:

$$\theta_t \geq 2\sqrt{0.017^2 + 0.02^2} + 2 \times 0.033 = 0.092 \text{ (mrad)} \tag{17}$$

Considering that only the brightness of the half-center area of the laser spot is sufficient to enable the focal plane of the APD laser detector to detect an extremely small of reflected echo, the design value of the laser beam divergence angle θ_t should be 0.2 mrad after leaving a sufficient design margin.

According to the tests conducted in this study, the laser will arrive at the target at the moment of 1.6 ms after imaging. As a result, it creates a beam pointing error, which must be smaller than the beam divergence θ_t so that the laser can cover the target.

$$\theta_t \geq \tan^{-1}\left(v_p \times 0.0016 \div 30,000\right) \tag{18}$$

In Equation (18), v_p represents the velocity component of the target in the direction perpendicular to the camera's optical axis. After calculation, v_p must be less than 3.75 km/s. Mostly, the debris target will not collide with the spacecraft when the velocity component perpendicular to the camera's optical axis is greater than 3.75 km/s.

The laser rangefinder adopts a single-photon detection form, and the sensitivity of the laser-receiving focal plane is very high [19], which can reach the level of single-photon response.

4.1. Design of Optical Lens for Laser Collimation

The design result of the optical system of the lens for laser collimation is shown in Figure 8, and the parameters are listed in Table 2.
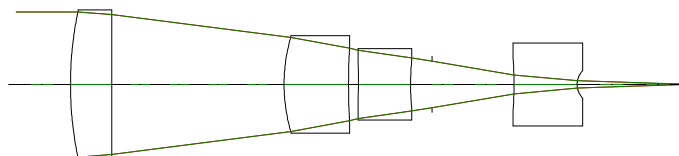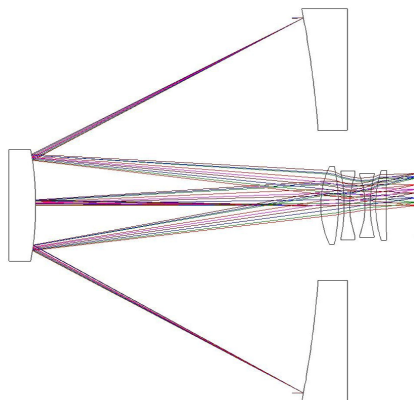

Figure 8. Optical system of the lens for laser collimation.

Table 2. Parameters of the optical system of the lens for laser collimation.

Parameters	Values
Wavelength	1064 nm $\pm$ 2 nm
Laser incidence divergence angle	3.5° (61.1 mrad)
Laser emission divergence angle	0.2 mrad
Focal length	160 mm
Maximum optical aperture	10.3 mm

4.2. Design of Laser-Receiving Optical Lens

The laser-receiving optical lens adopts an RC-type structure. The designed optical system of the laser-receiving lens is shown in Figures 9 and 10.

Figure 9. Optical system of the laser-receiving lens.
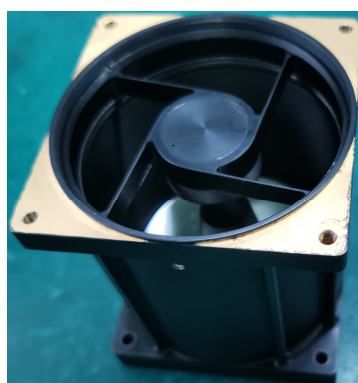
Figure 10. Image of the optical objective lens used in the laser-receiving system.

The total length of the laser-receiving optical system (from the front-end face of the secondary mirror to the image plane) is 160 mm, the rear working distance is 20 mm, and the maximum optical diameter is Ø150 mm. The parameters of the laser-receiving optical system are shown in Table 3.

**Table 3.** Parameters of the laser-receiving optical system.

Parameters	Values
Wavelength	1064 nm $\pm$ 2 nm
Focal length	360 mm
Field of view	2.04° × 2.04°
Relative aperture	2.4
Distortion	<0.8%
Detector pixel	128 × 128, pixel size is 100 μm × 100 μm

4.3. Design of High-Speed Deflection Mirror System

The high-speed deflection mirror system includes a two-dimensional FSM, a two-dimensional reflector driver, and a controller [20]. The two-dimensional FSM is placed in the optical path of the laser rangefinder to quickly deflect in the two-dimensional directions; the laser optical axis can be adjusted in two dimensions. The performance indicators of the high-speed deflection mirror system are as follows [21]:

(a)   Range of deflection: ≥2° × 2°;
(b)   Angular resolution: ≤2 μrad under load conditions;
(c)   Mirror size: Φ12.5 mm × 5 mm;
(d)   Swing frequency: ≥1000 Hz under load conditions.

When a target enters the field of view of the high-resolution telephoto camera, the target detection system intelligently recognizes the target and calculates its sight angles. The composition of the high-speed deflection mirror system is shown in Figure 11. The high-speed deflection mirror system communicates with the outside through the RS422 interface to obtain the sight angles of the target, perform two-dimensional calculation, control the high-speed adjustment of the deflection mirror optical axis to make the laser optical axis point at the target, and quickly measure the distance to the target.
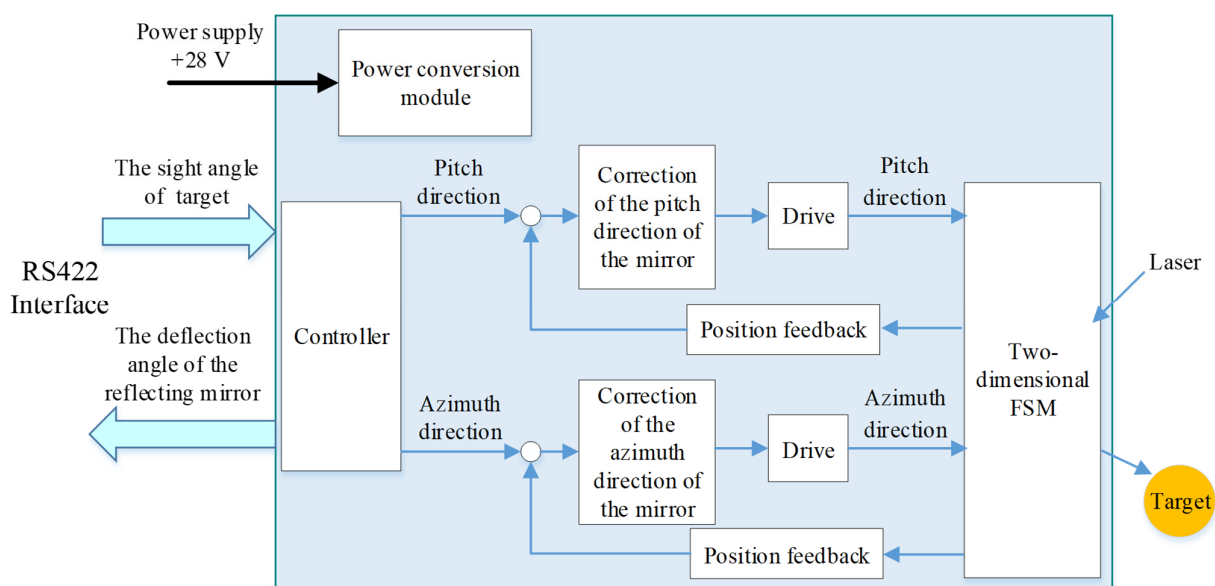
Figure 11. Composition of the high-speed deflection mirror system.

The selected high-speed deflection mirror is a piezoelectric ceramic two-dimensional FSM, consisting of piezoelectric ceramics and a unit for driving and control. The driving and control unit drives the piezoelectric ceramics to enable small rotations of the optical mirror around the *X*- and *Y*-axes, thus achieving precise control of the laser beam. It has the characteristics of high-precision and high-frequency response, as well as good stability and reliability [22].

The driving and control unit controls the FSM according to the instructions issued by the terminal control system and achieves control of the aiming angle of the laser beam through the deflection of the FSM. Meanwhile, the actual deflection angle of the laser beam can be detected using a kind of photodetector, thereby achieving high precision and closed-loop control [23].

The adopted two-dimensional FSM is a customized commercial product and is shown in Figure 12. The main indicators of the product are as follows:

(a) Range of deflection: 35 mrad;
(b) Angular resolution: 1 μrad;
(c) Repeated location accuracy: 1 μrad;
(d) Linearity: 0.05%;
(e) Temperature range: −30~80 °C.

Figure 12. Two-dimensional FSM.

5. Analysis of Location Error Composition and Calculation of Location Accuracy

Error analysis is a foundation for reducing errors. Only by conducting a detailed analysis of the composition and sources of errors can the main links and sources that cause errors be identified, and then the errors in each link of the target location can be reasonably allocated. Effective methods and approaches to reduce target location errors have been proposed.

Based on Equation (10), the following equation can be used to find the partial differential of X_A:

$$\delta X_A = \frac{\partial X_A}{\partial X_C}\delta X_C + \frac{\partial X_A}{\partial L}\delta L + \frac{\partial X_A}{\partial \phi}\delta\phi + \frac{\partial X_A}{\partial \omega}\delta\omega + \frac{\partial X_A}{\partial k}\delta k + \frac{\partial X_A}{\partial f}\delta f + \frac{\partial X_A}{\partial x}\delta x + \frac{\partial X_A}{\partial y}\delta y + \frac{\partial X_A}{\partial x_0}\delta x_0 + \frac{\partial X_A}{\partial y_0}\delta y_0 \quad (19)$$

According to Equation (19) and the error synthesis theory, the error of this target location method in the *X* direction of the satellite coordinate system is calculated as follows:

$$M_X = \sqrt{ \begin{array}{l} \left(\frac{\partial X_A}{\partial X_C}\delta X_C\right)^2 + \left(\frac{\partial X_A}{\partial L}\delta L\right)^2 + \left(\frac{\partial X_A}{\partial \phi}\delta\phi\right)^2 + \left(\frac{\partial X_A}{\partial \omega}\delta\omega\right)^2 + \left(\frac{\partial X_A}{\partial k}\delta k\right)^2 + \left(\frac{\partial X_A}{\partial f}\delta f\right)^2 \\ + \left(\frac{\partial X_A}{\partial x}\delta x\right)^2 + \left(\frac{\partial X_A}{\partial y}\delta y\right)^2 + \left(\frac{\partial X_A}{\partial x_0}\delta x_0\right)^2 + \left(\frac{\partial X_A}{\partial y_0}\delta y_0\right)^2 \end{array} } \tag{20}$$

$$M_X = \sqrt{M_{XC}^2 + M_L^2 + M_\phi^2 + M_\omega^2 + M_k^2 + M_f^2 + M_x^2 + M_y^2 + M_{x_0}^2 + M_{y_0}^2} \tag{21}$$

Similarly, the error of this target location method in the Y and Z directions of the spacecraft coordinate system is calculated as follows:

$$M_Y = \sqrt{ \begin{array}{l} \left(\frac{\partial Y_A}{\partial Y_C}\delta Y_C\right)^2 + \left(\frac{\partial Y_A}{\partial L}\delta L\right)^2 + \left(\frac{\partial Y_A}{\partial \phi}\delta\phi\right)^2 + \left(\frac{\partial Y_A}{\partial \omega}\delta\omega\right)^2 + \left(\frac{\partial Y_A}{\partial k}\delta k\right)^2 + \left(\frac{\partial Y_A}{\partial f}\delta f\right)^2 \\ + \left(\frac{\partial Y_A}{\partial x}\delta x\right)^2 + \left(\frac{\partial Y_A}{\partial y}\delta y\right)^2 + \left(\frac{\partial Y_A}{\partial x_0}\delta x_0\right)^2 + \left(\frac{\partial Y_A}{\partial y_0}\delta y_0\right)^2 \end{array} } \tag{22}$$

$$M_Z = \sqrt{ \begin{array}{l} \left(\frac{\partial Z_A}{\partial Z_C}\delta Z_C\right)^2 + \left(\frac{\partial Z_A}{\partial L}\delta L\right)^2 + \left(\frac{\partial Z_A}{\partial \phi}\delta\phi\right)^2 + \left(\frac{\partial Z_A}{\partial \omega}\delta\omega\right)^2 + \left(\frac{\partial Z_A}{\partial k}\delta k\right)^2 + \left(\frac{\partial Z_A}{\partial f}\delta f\right)^2 \\ + \left(\frac{\partial Z_A}{\partial x}\delta x\right)^2 + \left(\frac{\partial Z_A}{\partial y}\delta y\right)^2 + \left(\frac{\partial Z_A}{\partial x_0}\delta x_0\right)^2 + \left(\frac{\partial Z_A}{\partial y_0}\delta y_0\right)^2 \end{array} } \tag{23}$$

The location error is calculated as follows:

$$M = \sqrt{M_X^2 + M_Y^2 + M_Z^2} \tag{24}$$

Based on the sources of errors together with the actual parameters of the camera, the input parameters for calculating the target location accuracy are as follows:

1. The location errors of point C at the camera photography center—δ_{XC}, δ_{YC}, and δ_{ZC}—are determined by the accuracy of the position information output by the position system (such as GPS) of the spacecraft (satellites, etc.) itself. δ_{XC}, δ_{YC}, and δ_{ZC} are determined to be 3 m.

2. δL represents the laser-ranging error of the target, with an error value of 14 m and an L value of 30 km.

3. The measurement errors of the pose angles in the external orientation elements are $\delta\varphi$, $\delta\omega$, and δk. In this target location accuracy analysis model, the measurement accuracy of the spacecraft pose measurement system based on star sensors and the stability accuracy of the spacecraft are comprehensively considered. The measurement errors of the pitch angle, roll angle, and yaw angle are all 18″ at approximately 0.005°.

4. For the high-resolution optical camera on the spacecraft, the average angles between the main optical axis and the three coordinate axes of the spacecraft coordinate system are all 45°. When calculating location accuracy, all three azimuth angles are taken to be 45°.

5. f is the focal length of the camera, which is 862.5 mm. δf is the focal length calibration error, which is 0.1 mm.

6. x and y are the coordinate values of image point a on the image coordinate system. Based on the size of the imaging detector, the maximum value of x-x_0 and y-y_0 is calculated to be 6.9 mm. δx and δy are the measurement errors of image point a, which are caused by factors such as target recognition errors and image distortion. After comprehensive consideration, they are determined to be all 10 μm.

7. The calibration error of the main point of the internal orientation elements is 10 μm for δx_0 and δy_0.

The above parameters are substituted into Equations (20) and (22)–(24), and MATLAB 2020a calculation software is used to calculate the target location accuracy. The summary of location errors is shown in Table 4.

Table 4. Summary of location errors (unit: m).

δL		M_{XC}	M_{YC}	M_{ZC}	M_L	M_φ	M_ω	M_k	M_f	M_x	M_y	M_{x0}	M_{y0}	$M_X/M_Y/M_Z$	M
	X	3	0	0	6.92	1.29	1.32	0.02	0.02	0.05	0.30	0.05	0.30	7.78	
14	Y	0	3	0	10.0	0	1.83	0	0.03	0.17	0.17	0.17	0.17	10.61	15.3
	Z	0	0	3	6.93	1.29	1.32	0.02	0.02	0.30	0.05	0.30	0.05	7.78	

From Table 4, it can be seen that the location errors (M_{x0}, M_{y0}, M_f, M_x, and M_y) caused by the calibration error of the camera's internal orientation elements and the measurement error of each image point are all less than 0.5 m, accounting for a small proportion of the total location error and, thus, having little impact on it.

The location error caused by the measurement error of the pitch angle φ and the roll angle ω of the camera pose is also less than 2 m, and the measurement error of the yaw angle k has no effect on the target location accuracy.

The location error of the spacecraft itself is added 1:1 to the total target location error, and it accounts for a large proportion of the total error. Improving the location accuracy of the spacecraft itself is one of the ways to reduce the target location error.

Because the laser-ranging error is 14 m, it is calculated that the location error caused by the laser-ranging error is the largest. Therefore, improving the ranging accuracy of the laser rangefinder is one of the main ways to enhance target location accuracy.

According to the comprehensive summary of location error data presented in Table 4, when the target distance is 30 km, the target location accuracy can reach 15.3 m.

According to the tests conducted in this study, the target image can be obtained in 0.5 ms, the time of the FSM deflection is about 1 ms, the time of laser transmission is 0.2 ms, the distance information can be obtained in 0.5 ms after the reflected laser is received, and the target location calculation can be completed in 0.5 ms. Thus, the total time of the target location is 2.7 ms. When encountering a space target with a relative motion speed of 8 km/s (the velocity component perpendicular to the camera's optical axis is less than 3.75 km/s), the target has moved 21.6 m by the time the calculation of target location is completed.

$$M_{\Delta T} = \sqrt{15.3^2 + 21.6^2} = 26.5 \ (\text{m}) \tag{25}$$

Therefore, considering the time delay of target information acquisition and location calculation, $M_{\Delta T}$ (the location error of high-speed moving targets considering time delay) is about 26.5 m (with a relative motion velocity of 8 km/s and the velocity component perpendicular to the camera's optical axis is less than 3.75 km/s).

6. In-Orbit Target Location Experiment

The target location system was launched into orbit after completing the assembly and testing it on the ground; in-orbit observation and location experiments were carried out on a cooperative target satellite. As shown in Figure 13, the target location system was installed on satellite *B*. Satellite *B* gradually approached satellite *A* slowly, and when the distance between them was 30 km, it began to observe, photograph, and measure the distance to satellite *A*; the location of satellite *A* was obtained using the method described in this paper.
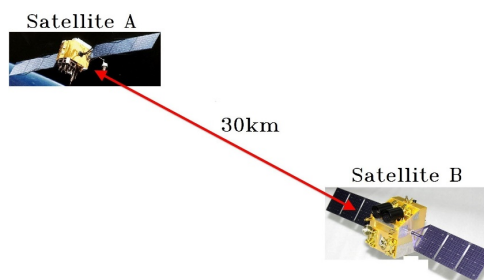
Figure 13. Schematic diagram of the cooperative target observation and location experiment.

Figure 14 shows an image obtained after shooting of the camera installed on satellite *B*; the image point of satellite *A* is located in the middle-left upper part of the image. The pixel coordinates of the image point *a* of satellite *A* on the image are (1571, 1224), and the origin of the pixel coordinate system is located at the upper left corner of the image. The coordinate value (x, y) of the target image point *a* in the image coordinate system was calculated to be (-1.646 mm, 0.952 mm).
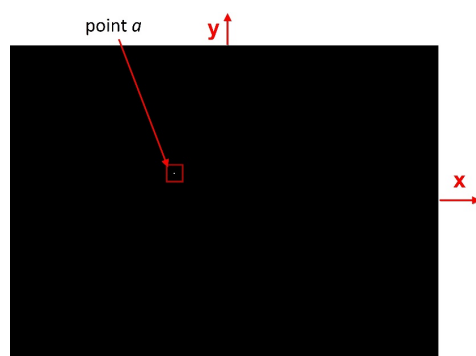

Figure 14. An image of the cooperative target, satellite *A*, captured in orbit.

The relevant parameters used for the target location calculation at the time of shooting are shown in Table 5.

Table 5. Parameters of the in-orbit location test.

Parameters	X_C	Y_C	Z_C	L	φ	ω	k	x_0	y_0
Values	1.1 m	-0.3 m	0.2 m	28,646 m	65.051°	$-17.615°$	25.133°	10 μm	7 μm

By substituting the above data into Equation (10), the coordinates (X_A, Y_A, Z_A) of the target point *A* (satellite *A*) in the satellite coordinate system W-xyz of satellite *B* were calculated to be (24,725, -8660, $-11,589$), with the unit in m.

The ephemeris data of satellite *B* at the time of shooting were obtained, and the coordinate origin of the satellite coordinate system Wxyz of satellite *B* was calculated to be (4,021,165.1, 3,639,908.7, 4,374,130.3) in the Earth-Centered, Earth-Fixed (ECEF) coordinate system, with the unit in m. Through coordinate transformation, the coordinates of the target point *A* in the ECEF coordinate system after target location calculation were obtained as (4,001,914.9, 3,655,833.7, 4,360,114.2).

The true coordinates of the target point *A* in the ECEF coordinate system at the time of shooting were calculated from the ephemeris data of satellite *A* to be (4,001,917.3, 3,655,846.4, 4,360,108.2).

By comparing the coordinates of the target point *A* obtained from the target location calculation with its true coordinates, the location error of the target point *A* was calculated to be 14.3 m when the relative velocity is small between satellite *A* and satellite *B*.

$$\sqrt{(4,001,917.3 - 4,001,914.9)^2 + (3,655,846.4 - 3,655,833.7)^2 + (4,360,108.2 - 4,360,114.2)^2} = 14.3 \text{ (m)} \qquad (26)$$

7. Conclusions

In response to the demand for quickly and accurately locating high-speed moving debris targets in space, a collinear equation was established based on the photographic imaging principle of target image acquisition and the precise distance of such a target. Then, a model for spatial target location was established based on the inner and outer orientation elements of the camera and the distance of the target. An equation for calculating the geographic coordinates of the target points was derived. A visible-light telephoto high-resolution camera and a laser rangefinder were designed for target location. A method for rapid ranging of spatial high-speed moving targets by incorporating fast steering mirror deflection into the laser rangefinder was proposed, which can further rapidly and accurately locate high-speed moving targets. The composition of the target point location error was analyzed, and an equation for calculating the target point location error was deduced. According to the actual component of each error and the error synthesis theory, the location accuracy of a high-speed moving target (with a relative motion velocity of 8 km/s and the velocity component perpendicular to the camera's optical axis is less than 3.75 km/s) was calculated to be 26.5 m, and the main suggestions for improving the target location accuracy were offered. In-orbit technical verification was conducted, and the geographical coordinate value of the cooperative satellite target was obtained using the proposed target location method.

Existing space target location technology usually needs multiple measurements of the same target, and the location accuracy of such a target is poor. The research work described in this paper can quickly determine the location of high-speed moving targets over long distances through one imaging measurement and achieve high location accuracy. However, the field of view of the high-resolution camera used for this target location method is too small, and the high-speed moving target stays in the field of view for too short a time, so it is impossible to obtain the high-precision continuous motion trajectory of the target over a long duration. Moreover, the proposed target location method has high requirements regarding the accuracy of the laser rangefinder.

The research described in this paper provides a theoretical basis and a method for solving the practical needs of rapid location of high-speed moving targets in space and has value as a reference for improving location accuracy.

Author Contributions: Investigation, resources, conceptualization, and writing—original draft preparation, K.S.; methodology and investigation, H.Y.; supervision, J.P.; project administration, Y.M.; methodology, H.Z. All authors have read and agreed to the published version of the manuscript.

Institutional Review Board Statement: Not applicable.

Informed Consent Statement: Not applicable.

Data Availability Statement: Some data, models, and codes that support the findings of this study are available from the corresponding author upon reasonable request.

Conflicts of Interest: The authors declare that they have no known competing financial interests or personal relationships that could have appeared to influence the work reported in this paper.

References

1. Klinkrad, H. Large satellite constellations and related challenges for space debris mitigation. *J. Space Saf. Eng.* **2017**, *4*, 59–60. [CrossRef]
2. Wang, X.; Li, J.; An, W. A Novel Method of Locating GEO Objects with Space-Based Optical Short Arcs Observation and the Geometric of Precision for Initial Orbit Determination. *Aerosp. Control* **2012**, *30*, 46–50.
3. Wu, Y.; Yu, F.; Liu, J. Double Line-of-Sight Cooperative Location Algorithm for Non-Cooperative Targets in Approaching Process. *J. Northwestern Polytech. Univ.* **2024**, *42*, 197–204. [CrossRef]
4. Wu, T.X.; Wen, M.X.; Wang, Y.M. Research on monostation passive location technology based on infrared tracking system. *Opt. Eng.* **2022**, *61*, 093103. [CrossRef]
5. Zhao, X.; Chen, Z.; Wang, M.; Wang, J. Maritime Target Recognition and Location System Based on Lightweight Neural Network. *Electronics* **2023**, *12*, 3292. [CrossRef]
6. Sun, H.; Jia, H.; Wang, L.; Xu, F.; Liu, J. Systematic Error Correction for Geo-Location of Airborne Optoelectronic Platforms. *Appl. Sci.* **2021**, *11*, 11067. [CrossRef]
7. Liu, C.; Ding, Y.; Zhang, H.; Xiu, J.; Kuang, H. Improving Target Geolocation Accuracy with Multi-View Aerial Images in Long-Range Oblique Photography. *Drones* **2024**, *8*, 177. [CrossRef]
8. Cai, Y.; Zhou, Y.; Zhang, H.; Xia, Y.; Qiao, P.; Zhao, J. Review of Target Geo-Location Algorithms for Aerial Remote Sensing Cameras without Control Points. *Appl. Sci.* **2022**, *12*, 12689. [CrossRef]
9. Zhang, X.; Yuan, G.; Zhang, H.; Qiao, C.; Liu, Z.; Ding, Y.; Liu, C. Precise Target Geo-Location of Long-Range Oblique Reconnaissance System for UAVs. *Sensors* **2022**, *22*, 1903. [CrossRef]
10. Xu, C.; Huang, D.; Liu, J. Target location of unmanned aerial vehicles based on the electro-optical stabilization and tracking platform. *Measurement* **2019**, *147*, 106848. [CrossRef]
11. Taghavi, E.; Song, D.; Tharmarasa, R.; Kirubarajan, T. Geo-registration and Geo-location Using Two Airborne Video Sensors. *IEEE Trans. Aerosp. Electron. Syst.* **2020**, *56*, 2910–2921. [CrossRef]
12. Liu, Z.; Zhang, X.; Kuang, H.; Li, Q.; Qiao, C. Target Location Based on Stereo Imaging of Airborne Electro-Optical Camera. *Acta Opt. Sin.* **2019**, *39*, 1112003.
13. Iwasa, T.; Okumura, Y. Long depth-range measurement for fringe projection photogrammetry using calibration method with two reference planes. *Opt. Lasers Eng.* **2022**, *151*, 106940. [CrossRef]
14. Li, Z.; Wu, E.; Pang, C.; Du, B.; Tao, Y.; Peng, H.; Zeng, H.; Wu, G. Multi-beam single-photon-counting three-dimensional imaging lidar. *Opt. Express* **2017**, *25*, 10189–10195. [CrossRef] [PubMed]
15. Masoomi, N.; Zakery, A.; Afkhami, M. Design of a compact multispectral telescope consisting of a Cassegrain telescope and a concave elliptical grating. *Appl. Opt.* **2024**, *63*, 2195–2203. [CrossRef]
16. Xing, Y.; Li, H.; Cui, X.; Sun, G.; Zhu, L. Delayed-focus micro-angle measurement optical system based on structural segregation. *Appl. Opt.* **2024**, *63*, 5569–5577. [CrossRef]
17. Wang, N.; Wang, R.; Mo, D.; Li, G.; Zhang, K.; Wu, Y. Inverse synthetic aperture LADAR demonstration: System structure, imaging processing, and experiment result. *Appl. Opt.* **2018**, *57*, 230–236. [CrossRef]
18. Wang, L.; Yin, Z.; Lu, T.; Yi, Y.; Dong, X.; Dai, Y.; Bu, Z.; Chen, Y.; Wang, X. 1064 nm rotational Raman polarization lidar for profiling aerosol and cloud characteristics. *Opt. Express* **2024**, *32*, 14963–14977. [CrossRef]
19. Zhang, H.; Liu, J.; An, Q.; Wang, J. Time Coding-Based Single-Photon-Counting Lidar for Obtaining Spatial Location. *Photonics* **2023**, *10*, 457. [CrossRef]
20. Tu, J.; Wang, M.; Zhang, L. A shortcut to marking 3D target curves on curved surface via a galvanometric laser scanner. *Chin. J. Aeronaut.* **2019**, *32*, 1555–1563. [CrossRef]
21. Sun, N.; Wang, Y.; Wu, Y.; Liu, J. High-Precision Tracking of Free-Space Optical Communication System on Mobile Platforms. *Photonics* **2024**, *11*, 900. [CrossRef]
22. Han, W.; Shao, S.; Zhang, S.; Tian, Z.; Xu, M. Design and modeling of decoupled miniature fast steering mirror with ultrahigh precision. *Mech. Syst. Signal Process.* **2022**, *167*, 108521. [CrossRef]
23. Chang, Q.; Chen, W.; Liu, J.; Yu, H.; Deng, J.; Liu, Y. Development of a novel two-DOF piezo-driven fast steering mirror with high stiffness and good decoupling characteristic. *Mech. Syst. Signal Process.* **2021**, *159*, 107851. [CrossRef]